Full Length Article

Pulsed laser melting of implant amorphized Si$_{1-x}$Ge$_x$ thin films

Jesse A. Johnson II [a,*], David Brown [a], Emily Turner [a], Chris Hatem [b], Bruce Adams [c], Xuebin Li [c], Kevin S. Jones [a]

[a] Department of Materials Science & Engineering, University of Florida, Gainesville, FL 32608
[b] Applied Materials – Varian Semiconductor Equipment, Gloucester, MA 01930
[c] Applied Materials, Sunnyvale, CA 94085

A B S T R A C T

Nanosecond pulsed laser annealing using a frequency doubled Nd:YAG laser (λ = 532 nm) was performed on undoped implant amorphized Si and 40 nm Si$_{1-x}$Ge$_x$ epitaxial thin films ranging from x = 0.1 to 0.5. Ge$^+$ implants were used to create ∼ 15 nm thick surface amorphous layers. The microstructural evolution of the layers was investigated for laser powers that ranged from the sub-melt, partial amorphous layer melt, full amorphous layer melt, to full epi-layer melt regimes. Time resolved reflectometry and transmission electron microscopy was used to couple the impact of melt dynamics with resulting microstructures and to determine processing benchmarks as a function of Ge concentration. It was shown that for the right combination of power and amorphous layer thickness, defect free regrowth is possible. At melt depths $\geq$ 22 nm for the Si$_{0.7}$Ge$_{0.3}$ films, it was found that progressive liquid/solid interface roughening during solidification led to lateral germanium segregation coupled with the formation of dislocation half loops and dislocation loop clusters at the surface. These results are important for the exploration of pulsed laser melting of Si$_{1-x}$Ge$_x$ for CMOS source/drain contact and channel strain engineering applications.

1. Introduction.

Since the 90 nm logic technology node, the use of Si$_{1-x}$Ge$_x$ in source/drain (S/D) applications to create a strained Si channel has been a crucial component in CMOS technology [1]. Si$_{1-x}$Ge$_x$ straining has allowed pMOS transistors to match performance gains in nMOS by increasing the hole mobility [1]. Additionally, Si$_{1-x}$Ge$_x$ in the S/D has a positive effect on the interfacial contact resistance at the metal/semiconductor interface due to Schottky barrier lowering with increased Ge concentration [2]. As a result, Si$_{1-x}$Ge$_x$ in the S/D region remains a vital component in pMOS, and further improvements in thermal processing, dopant activation, and contact metallization of Si$_{1-x}$Ge$_x$ are needed [3–5].

It is well known that sub-µs pulsed laser melting of Si is one of the most effective methods for maximizing dopant activation [6–9]. Despite integration challenges such as non-uniform absorption caused by pattern effects, the opportunities afforded by laser melting have continued to fuel interest in its application in CMOS technology development. It is well established that ion implantation can be used to amorphize Si to a controllable depth [10,11]. As a result, many studies have been dedicated to an approach termed laser thermal processing (LTP) of implant amorphized Si which take advantage of the reduced melting temperature of amorphous Si relative to crystalline Si [12,13]. This reduction in melting temperature, combined with the shallow optical absorption of the laser which localizes heating to the surface, allows for the pulsed laser melting process to operate within thermal budget constraints of CMOS devices. Related phenomena such as explosive crystallization, fluence thresholds for defect free epitaxial regrowth, and controllable junction formation have also been studied in Si [14–17].

More recently the incorporation of Si$_{1-x}$Ge$_x$ into heterojunction bipolar transistor and logic devices has led to a number of studies investigating LTP of Si$_{1-x}$Ge$_x$, including quantification of the Ge velocity dependent segregation coefficient and the application of graded Si$_{1-x}$Ge$_x$ layers for strained Si applications [1,18–22]. The increase in parasitic resistances caused by aggressive CMOS scaling has resulted in a growing number of studies applying LTP of implant amorphized Si$_{1-x}$Ge$_x$ S/D to state-of-the-art devices [23,24]. Furthermore, the reduced melting temperature of Si$_{1-x}$Ge$_x$ alloys relative to Si allows for melt propagation to be confined to well defined depths. The results have been very promising and show LTP has the potential to meet thermal budget and

doping requirements for existing and future technology nodes. Surprisingly, there are few microstructural studies of the effects of LTP on implant amorphized $Si_{1-x}Ge_x$. Studies involving LTP of amorphized $S_{1-x}Ge_x$ from As- and Ga-doping via implantation have suggested Ge and dopant segregation can occur and this can alter the microstructure [25–27]. To better understand the microstructural evolution upon laser thermal processing and to decouple dopant effects, a comprehensive study of LTP in undoped amorphized $Si_{1-x}Ge_x$ is needed. This paper investigates the effect of laser parameters on melt propagation and resulting microstructures of implant amorphized $Si_{1-x}Ge_x$ layers as a function of Ge concentration. A combination of time resolved reflectometry and transmission electron microscopy is used to explain how these layers evolve after laser melting and recrystallization.

2. Materials and methods

2.1. $Si_{1-x}Ge_x$ epitaxy and ion implantation

40 nm thick undoped $Si_{1-x}Ge_x$ epi layers (x = 0.1, 0.3, and 0.5) were grown on blanket 300 mm $(1\,0\,0)$ Si wafers using an Applied Materials Centura® reduced pressure chemical vapor deposition (CVD) system. Prior to deposition, native oxide on the Si wafers was removed in the SiCoNi™ chamber and transferred to the CVD chamber without breaking vacuum. Dichlorosilane (SiH_2Cl_2) and Germane (GeH_4) were used as precursors for Si and Ge respectively, with H_2 used as a carrier gas. Growth temperatures were within the range of 600–650 °C and were gradually lowered with increasing Ge concentration to promote strained growth of the $Si_{1-x}Ge_x$ layers. All layers were pseudomorphic, with the exception of the 50% Ge layers which were partially relaxed. Amorphizing implants were performed on all epi samples as well as a Si control sample. All wafers were implanted at room temperature with a 10 keV Ge^+ 1×10^{14} cm^{-2} implant resulting in a 10–15 nm amorphous layer depending on the Ge content. The amorphous layer thickness decreased with increasing Ge content due to the decrease in ion projected range.

2.2. Laser irradiation and time resolved reflectometry (TRR)

Samples were irradiated with a Q-switched frequency doubled Nd: YAG laser ($\lambda = 532$ nm). Fig. 1 is a schematic of the pulsed laser and reflectometer setup. The beam path was comprised of pulse stretching and beam-shaping optics including a pair of micro-lens arrays, and a square aperture imaged the beam to a 9x9 mm^2 square at the target. The optics are such that a uniform top-hat profile with less than 3% deviation is created over the entire 9×9 mm^2 area to avoid the need for scanning. A pair of lasers chained together resulted in a roughly Gaussian time profile with a pulse length of 32 ns full width at half maximum. The lasers operate with a repetition rate of 5 Hz; however, for these studies

only a single pulse was used. A fluence range of 185–728 mJ/cm^2 was used, which was sufficient to cover the sub-melt to liquid phase epitaxy regimes in all sample sets. The standard deviation of energy density from pulse to pulse was measured to be less than 1.5%. Samples were placed in a vacuum chamber at a pressure of 1.3 torr and irradiated through an optical quartz window at room temperature.

TRR spectra were collected using a low power CW diode laser ($\lambda = 658$ nm) with 3 mm $\varnothing$ incident beam at near normal, and the reflected beam was collected using a Si PIN photodetector connected to a digitizing oscilloscope. Unless stated otherwise, the term 'reflectivity' is used to refer to the induced photovoltage of the reflected beam. The recording of the TRR spectra by the oscilloscope were triggered by a photodetector collecting the diffusely scattered light of the Nd:YAG laser pulse from the beam-shaping optics. In this investigation, because of the differences in reflectance between samples of varying Ge concentration, the initial collected photovoltage for all samples was set to 100 mV. Effectively, the collected TRR spectra are a measure of the change in reflectivity, allowing for direct comparison over all sample conditions and laser energy densities.

A description of the TRR technique has been reviewed before and is briefly described below [28]. The TRR approach employs the ability of a laser to penetrate a surface, and probe changes in reflectivity over the nanosecond time scale. For Si and Ge, the molten phase is metallic due to the delocalization of electrons, producing a higher reflectivity than the solid phase. Additionally, reflectivity is sensitive to temperature and increases with elevating temperatures. Fig. 2 is a schematic of the dynamics of an ideal pulsed laser melting event of implant amorphized $Si_{1-x}Ge_x$. Melting begins at the surface and a liquid/solid (l/s) interface propagates inward to a maximum melt depth before solidification propagates towards the surface. The maximum depth of the l/s interface is a function of energy density for a given pulse length, and the l/s
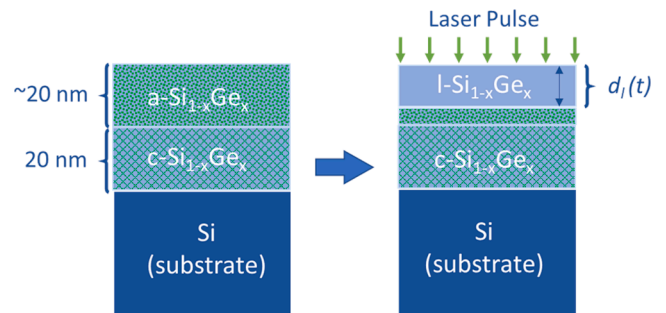

Fig. 2. Schematic of a pulsed laser melting event of an implant amorphized epitaxial $Si_{1-x}Ge_x$ layer.
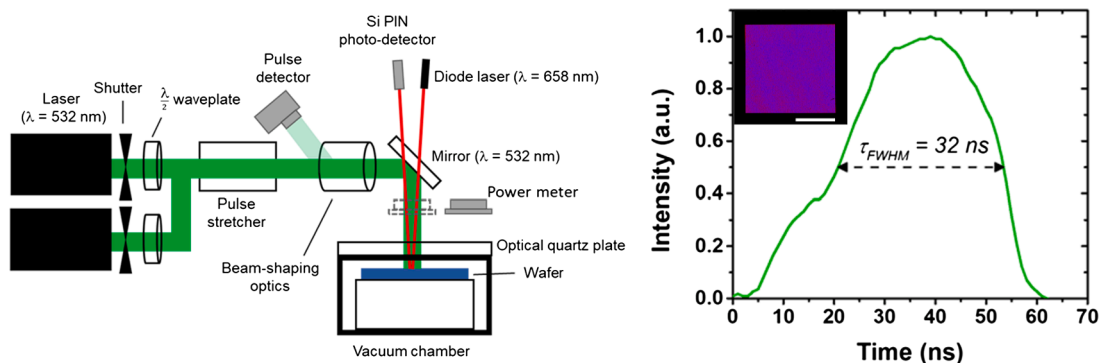

Fig. 1. Schematic of the 2nd harmonic Q-switched Nd:YAG laser system and reflectometer. Energy density is controlled by the waveplate, and the shutter allows for selection of single pulse anneals. The reflectometer is composed of a CW diode laser and Si PIN photodetector connected to a digitizing oscilloscope. The diode laser is focused on the center of the area irradiated by the Nd:YAG pulse. The temporal intensity profile is near-gaussian and the standard deviation of the cross-sectional energy distribution is $\pm$ 3%. The scale bar is 4 mm.

interface position is a function of time. When applied to a dynamic process such as pulsed laser melting, the reflection of a probing laser can detect the heating of a solid, propagation and solidification of a molten phase, and the subsequent crystallization of an initially amorphous phase. For Si in the solid state, the reflectivity is higher for the amorphous phase than crystalline, and polycrystalline-Si (pc-Si) possesses a reflectivity between that of single crystal-Si (sc-Si) and amorphous-Si (a-Si) at a wavelength of 633 nm [28]. For Ge in the solid state, it has been reported that the absolute reflectance of a-Ge and sc-Ge are nearly equivalent at wavelengths near 658 nm [29]. The optical properties of a-$Si_{1-x}Ge_x$ have not been reported in literature and is beyond the scope of this work, however, this study will empirically determine reflectivity trends as a function of Ge concentration and phase by supplementing with TEM.

2.2.1. Modeling of amorphous and crystalline Si melting

Modeling of the time dependent l/s interface position and temperature profile was used to help explain TRR spectra and resulting microstructures as fluence is increased from the amorphous to crystalline melting regime. The laser induced melt predictions (LIMP) program was used and works by solving the one-dimensional heat flow equation for energy deposited near the sample surface by a laser pulse [30]. The temporal pulse profile of the laser system, Fig. 1, was used along with material parameter profiles that include the temperature dependent physical and optical properties of the layers in the samples [31,32]. Due to the lack of reported values for a-$Si_{1-x}Ge_x$, melt dynamics of an a-Si/c-Si stack are extrapolated to observations in the implanted $Si_{1-x}Ge_x$ samples.

2.3. Microstructural characterization

TRR spectra were correlated as a function of energy density and Ge concentration with corresponding post-irradiation cross-sectional high-resolution TEM (X-TEM) micrographs. Lamellae were prepared using an FEI Helios NanoLab 600 dual beam FIB/SEM that utilized in situ Pt deposition prior to milling to protect the sample surface. An FEI Talos F200i S/TEM was used for high-resolution TEM and high angle annular dark-field (HAADF) STEM imaging, in addition to energy dispersive spectroscopy (EDS) for chemical depth profiling.

3. Results and discussion

For each set of samples, single pulse anneals were performed where the laser fluence was sequentially raised from a low value in the sub-melt regime to the fluence threshold necessary to achieve liquid phase epitaxy from the amorphous/crystalline (a/c) interface. A key focus of this study was to identify important pulsed laser processing benchmarks in terms of fluence such as the solid phase epitaxy regime, the onset of melt, and the threshold for liquid phase epitaxy. Melting of the amorphous layer occurs at temperatures below the equilibrium melting temperature of c-$Si_{1-x}Ge_x$, producing a melt that is highly undercooled leading to rapid re-solidification velocities. As laser fluence was increased from this regime, particular attention was paid to the dynamics of the (l/s) interface position relative to the a/c interface as temperatures approach and surpass the c-$Si_{1-x}Ge_x$ melting temperature. A crucial component of the implantation technique is to fully repair the damaged introduced into the lattice that can extend into the end-of-range (EOR) region beginning at the a/c interface. The roughness profile of the a/c interface can produce faulted liquid phase epitaxial regrowth, therefore, defect evolution and elimination as a function of fluence and melt depth is stressed.

3.1. Sub-melt to threshold for liquid phase epitaxial regrowth

TRR spectra ranging from sub-melt (≤ 247 mJ/cm^2) to full melting of the amorphous layer (≥ 284 mJ/cm^2) is shown in Fig. 3a. A plot of the

change in reflected intensity between the final and initial steady state reflectance (ΔR) as a function of laser fluence is shown in Fig. 3b. At energy densities below 272 mJ/cm^2 no melt is detected and the observed rise in reflectivity is due to the rapid heating of a-$Si_{0.7}Ge_{0.3}$. This rise in reflectivity is monotonic with time in the solid phase and is characteristic of all spectra collected below the melting point. The slight reduction in the final steady state reflectance seen in the 247 mJ/cm^2 spectrum indicates a conversion of amorphous material into crystalline. Comparison of the as-implanted cross-sectional TEM (XTEM) micrograph in Fig. 3c with the corresponding XTEM micrograph for the 247 mJ/cm^2 pulse, Fig. 3d, shows the layer is still amorphous and the decrease in reflectivity can be attributed to solid phase epitaxy at the a/c interface. The diffuse rings seen in the fast Fourier transform (FFT) of the top layer shown in the inset additionally confirms the absence of any crystallinity. Deviation from the monotonic rise in reflectivity of the TRR trace observed in the solid state is first seen at an energy density of 272 mJ/cm^2 and is attributed to the onset of melt on the surface. A more pronounced drop in the final steady-state reflectance is observed in the TRR trace, indicating a larger fraction of the amorphous layer recrystallized post irradiation. Due to the rough amorphous/crystalline (a/c) interface, XTEM in Fig. 3e shows un-melted amorphous pockets between polycrystalline and epitaxial $Si_{0.7}Ge_{0.3}$ at deeper regions of the a/c interface along with a textured grain at a shallower region, indicating the maximum melt depth only reached the shallower regions of the a/c interface. The FFT of the top layer showing the reciprocal space of the lattice clearly shows {111} rings indicative of the polycrystalline phase along with single crystal spots and streaking from the textured grain. As energy density is increased to 284 mJ/cm^2 the peak intensity of the TRR signal increases due to both the melt propagating deeper into the a-$Si_{0.7}Ge_{0.3}$ layer and to the increase in temperature of molten $Si_{0.7}Ge_{0.3}$. Spectra for the 284 & 308 mJ/cm^2 exhibit a saturation of the final steady state reflectance along with a significant drop in reflectance from the 272 mJ/cm^2 pulse. This signifies the threshold for liquid phase epitaxy has been reached (i.e. the liquid melt depth has reached the bottom of the amorphous layer and crystallization can occur from the single crystal substrate), verified by XTEM in Fig. 3f. Despite reaching the liquid phase epitaxy regime, the resulting single crystal is highly defective with micro-twins and stacking faults caused by imperfect seeding from the non-planar a/c interface. It is also possible the damage in the EOR region contributes to the nucleation of extended defects that propagate during liquid phase epitaxy. The FFT of the image in the [110] zone axis shows streaking in the ⟨111⟩ vectors and double diffraction spots which represents the presence of stacking faults and micro-twins respectively [33]. The trends in the TRR spectra highlight the decrease in reflectivity from the amorphous, polycrystalline, and epitaxial layers respectively. It can be seen in Fig. 3b that due to this trend, the inflection points of the ΔR plot correlate with the distinct solidification regimes between solid phase and liquid phase epitaxy.

Applying the TRR technique to amorphized epitaxial films with Ge concentrations $\leq 50\%$ shows a consistent hierarchy of reflectance between solid phases. An expanded ΔR plot that includes the process window to reach the threshold for liquid phase epitaxy for implanted $Si_{1-x}Ge_x$, where x = 0,0.1,0.3, and 0.5 is shown in Fig. 4a. The observed shift of the profiles in terms of fluence is a function of both melting temperature and pulsed laser absorption. Assuming homogeneous melting and solidification of $Si_{1-x}Ge_x$, the melting temperature of the alloy decreases linearly with increasing Ge concentration, leading to a reduction in deposited power necessary to induce melting [34]. However, the near overlapping of the $Si_{0.5}Ge_{0.5}$ and $Si_{0.7}Ge_{0.3}$ profiles suggest a non-linear change in optical absorption of the 532 nm laser pulse as a function of Ge concentration. In this case, a reduction in 532 nm absorption as Ge concentration is raised from 30% to 50% compensates for the reduction in the total deposited energy required to induce melting. For the 658 nm probing laser, the characteristic ΔR profile seen in the $Si_{0.7}Ge_{0.3}$ layers is observed in all other $Si_{1-x}Ge_x$ layers, although it can be seen that the magnitude in reflectivity difference between the amorphous and single
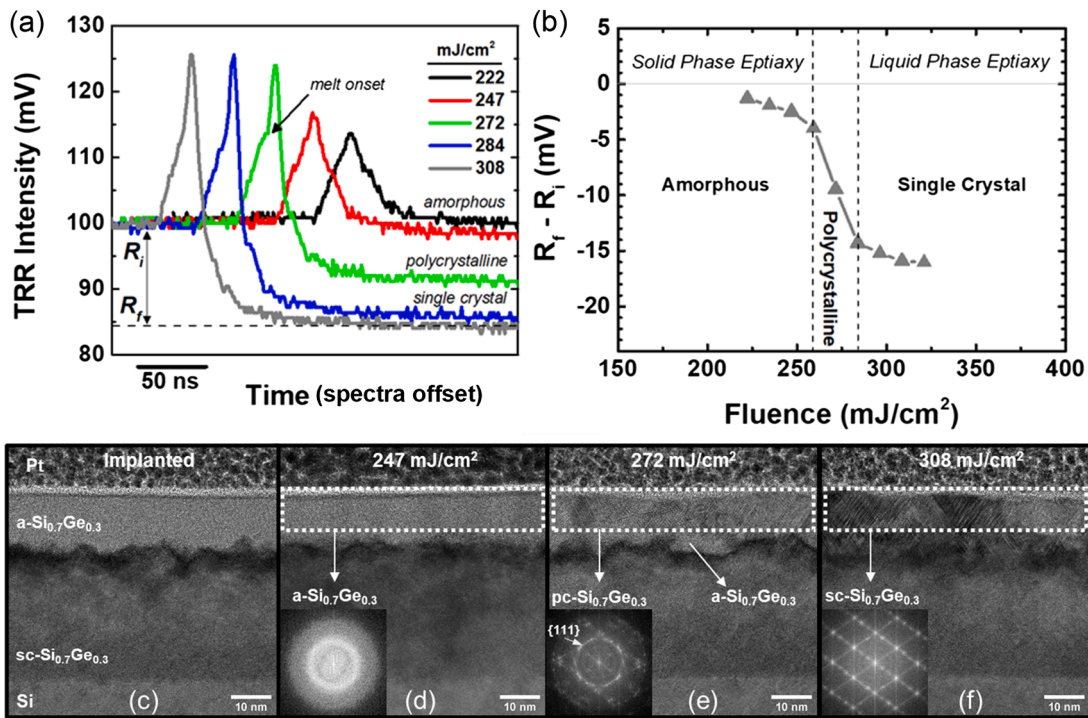
Fig. 3. TRR spectra for laser irradiated a-$Si_{0.7}Ge_{0.3}$ for increasing energy densities in the amorphous melting regime. Spectra are offset on the time axis to aid viewing **a)**. Plot of change in reflectance between final and initial steady-state reflectance as a function of fluence, **b)**. Cross-sectional TEM images illustrating the evolution of microstructure of implant amorphized $Si_{0.7}Ge_{0.3}$ subjected to single pulse anneals, from left to right, the as-implanted $Si_{0.7}Ge_{0.3}$ layer **c)**, 247 mJ/cm² pulse exhibiting sub-melt solid phase epitaxy **d)**, 272 mJ/cm² pulse exhibiting partial melt induced polycrystalline layer **e)**, and 308 mJ/cm² pulse exhibiting highly defective liquid phase epitaxy **f)**. The insets feature the Fast Fourier Transforms (FFT) of the top layer to confirm the microstructure.
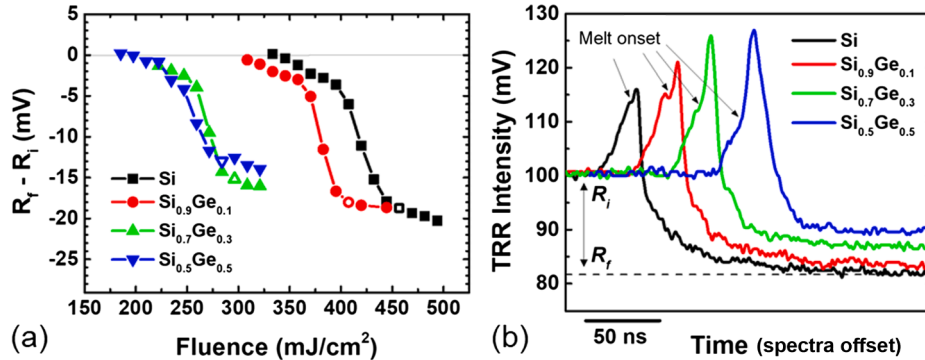

Fig. 4. Plot of change in steady state reflectance as a function of energy density for the $Si_{1-x}Ge_x$ films, (a). TRR spectra (offset on the time axis) corresponding to the single pulse threshold for liquid phase epitaxy for implant amorphized $Si_{1-x}Ge_x$, (b). The open symbols in figure (a) correspond to the spectra in (b).

crystal states decreases with increasing Ge concentration. TRR Spectra from the threshold for liquid phase epitaxy of each composition, designated by the open symbols in Figure, 4a, are shown in Fig. 4**b** and makes this difference more apparent. Recalling the study by Donovan et al., the absolute reflectance of single crystal Ge is nearly equivalent to amorphous Ge at 658 nm, so the ability to resolve solidification regimes diminishes with increasing Ge concentrations in SiGe alloys for this wavelength [29]. In contrast, the reflectivity difference between the liquid and the amorphous states is shown to increase with Ge concentration. More significantly, the difference between the hot-amorphous and liquid states diminishes with lower Ge concentrations, making it difficult to identify the onset of melt in Si-rich alloys by TRR spectra alone. Consequentially, the ΔR plot appears to be a more robust technique for identifying key process window benchmarks for pulsed laser annealing of shallow amorphous layers.

3.2. End-of-Range defect free liquid phase epitaxy

It has previously been shown for pulsed laser melting of implant amorphized single crystal silicon, that perfect recovery of the lattice requires melting of the damaged crystalline layer at the a/c interface [17,20,35]. The same is expected to be true of epitaxial $Si_{1-x}Ge_x$ on Si; however, pulsed laser melting of implant amorphized $Si_{1-x}Ge_x$ on Si has the added complexity of lattice mismatch, which may lead to strain relieving defects in the form of misfit dislocations, stacking faults, and other extended defects upon solidification.

As energy density is increased where temperatures approach and surpass the c-$Si_{0.7}Ge_{0.3}$ melting threshold, two competing processes occur that strongly influence the propagation of the liquid/solid interface. The first is the rapid solidification of the highly undercooled melt, and the second is the continued energy absorption by the specimen from

the laser pulse. Fig. 5a shows TRR spectra where fluence is increased passed the threshold for liquid phase epitaxy. The shoulder that appears on the 370 mJ/cm^2 spectra is the first indication that the isothermal melt stage has been reached, and while still highly undercooled, the temperature of the molten $Si_{0.7}Ge_{0.3}$ has begun to spike. A simulation of this stage using the Laser Induced Melt Predictions (LIMP) software package is demonstrated with a 20 nm a-Si layer in Fig. 5b. Amorphous Si is used because the temperature dependent optical and thermal properties of a-$Si_{1-x}Ge_x$ have yet to be reported in literature, while those of a-Si are well known. Although the thermal conductivity of c-$Si_{1-x}Ge_x$ alloys is known to increase with Ge concentration, it is reasonable to expect melt dynamics in implant amorphized $Si_{1-x}Ge_x$ to behave similar to amorphized Si. The time dependent melt depth and temperature profiles are shown, respectively, in the black and red traces, and the end of the laser pulse marked by the full width at half maximum is designated by τ_{FWHM}. A narrow process window exists where in the duration of the laser pulse, the temperature of the melt begins to spike while remaining below the 1687 K crystalline melting point. This is enough to slow the solidification velocity of the liquid/solid interface but not reverse direction. At higher energy densities, the crystalline solidification front propagates towards the surface until a sufficient amount of energy is absorbed to begin melting the newly solidified crystalline phase, as illustrated in Fig. 5c. This temperature and melt depth profile with a-Si is representative of the TRR spectra observed with the 469 mJ/cm^2 pulse on a-$Si_{0.7}Ge_{0.3}$ in Fig. 5a, where the secondary melt front reaches the EOR region. In Si, this melt phenomenon is explained by the reduced melting temperature of the amorphous state relative to crystalline (200 ± 50 K), combined with an order of magnitude decrease in thermal conductivity [15]. This results in having to overcome the rapid quenching of undercooled liquid-Si when the melt front reaches the a/c interface, producing initial solidification velocities upwards of 8–10 m/s as heat is transferred more efficiently towards the substrate.

The effect of increasing temperatures and melt depth as fluence is increased can be seen in the XTEM images of $Si_{0.7}Ge_{0.3}$ in Fig. 6. Resulting microstructures of a 420 mJ/cm^2 and 469 mJ/cm^2 pulse on $Si_{0.7}Ge_{0.3}$ are shown in Fig. 6a and 6b respectively. The insets display the FFT of the regrown layer to further illustrate the quality of lattice. A significant reduction in stacking faults seeding from the a/c interface and an elimination of twinning is seen in the 420 mJ/cm^2 pulse compared to the 308 mJ pulse, Fig. 3f, which was right at the threshold for epitaxial regrowth, and a complete elimination of stacking faults is achieved with a 469 mJ/cm^2 pulse. Due to the roughness of the a/c interface, the reduction of stacking faults and twins is caused by the secondary melt front reaching the shallow crystalline portions of the original a/c interface which had a variance of ~ 4 nm. Complete elimination of faults is only possible once the underlying crystalline $Si_{0.7}Ge_{0.3}$ of the original a/c interface has melted. Furthermore, no stacking faults or other extended defects were observed in the $Si_{0.7}Ge_{0.3}$ film or in the underlying Si substrate signifying minimal relaxation occurred during the anneal.

3.3. Melting to the $Si_{1-x}Ge_x/Si$ interface

The difference in melting temperatures of $Si_{1-x}Ge_x$ alloys relative to Si defines the optimal process window for pulsed laser melting of $Si_{1-x}Ge_x/Si$ heterostructures. For implant amorphized $Si_{1-x}Ge_x$ thin films, this process window is set between the energy density that produces EOR defect-free liquid phase epitaxy and melting to the $Si_{1-x}Ge_x/Si$ interface. Under the laser conditions used for this experiment, that energy density range fell between 469 and 728 mJ/cm^2 for the 40 nm thick $Si_{0.7}Ge_{0.3}/Si$ structures. TRR spectra for this regime are shown in Fig. 7. As fluence is increased and the melt front propagates past the EOR region in the $Si_{0.7}Ge_{0.3}$ film, the reflected intensity of the laser probe continues to rise until it reaches a saturation point with a 593 mJ/cm^2 pulse. A plateau in the time dependent position of the l/s interface traditionally occurs when the melt front reaches the interface of a material with a higher melting temperature. However, the 593 mJ/cm^2 pulse only produced a maximum melt depth of 30 nm in the 42 nm $Si_{0.7}Ge_{0.3}$ film, which indicates that the observed plateau is due to the onset of loss in depth resolution of the probing laser [36]. With increasing energy density, this characteristic plateau in the TRR traces continues to be observed up to the full melting of the epi-layer with slight increases in maximum intensity as a result of increasing temperatures. Despite the spatial homogeneity of the pulsed laser, it is well understood that the l/s interface produced by pulsed laser melting does not propagate as a perfect 2-dimensional plane due, in part, to microvariations in strain and composition, and in some cases, melt propagation through an alloy. The effects of l/s interface roughness can be seen in the resulting microstructures from the HR-TEM images shown in Fig. 8. The lateral variation in strain and/or z-contrast indicates that during solidification, progressive l/s interface roughening reaches a critical breakdown point where significant disorder is randomly incorporated into the lattice in localized clusters. Interestingly, the cluster formation was only observed in the $Si_{0.7}Ge_{0.3}$ thin films. Due to the thermodynamically driven segregation of Ge into the melt during solidification, the l/s interface at the maximum melt depth can be directly observed. The microstructure produced by partial epi-layer melting with the 617 mJ/cm^2 pulse in Fig. 8a. shows the onset of strain fields after a minimum of 15 nm of re-solidification from the maximum melt depth. The inset of Fig. 8a shows a higher magnification of the maximum l/s interface depth with a localized variance of ~ 1 nm, along with the atomically abrupt $Si_{0.7}Ge_{0.3}/Si$ interface. Full melting of the $Si_{0.7}Ge_{0.3}$ layer with the 728 mJ/cm^2 pulse shown in Fig. 8b. shows the onset of strain fields after a minimum of ~ 25 nm of solidification. These lengths were observed to be consistent upon examination of the entire electron transparent portion of the lamellae. HAADF-STEM imaging and EDS were used to determine if the lateral variations in contrast of the HR-TEM images had a Z-contrast component. The annular detector used in HAADF-STEM mode is set in a position where the inner angle collects little to no electrons scattered via diffraction producing an image with minimal strain contrast. The image is formed using thermal diffuse scattered electrons which are sensitive to atomic number, and the bright
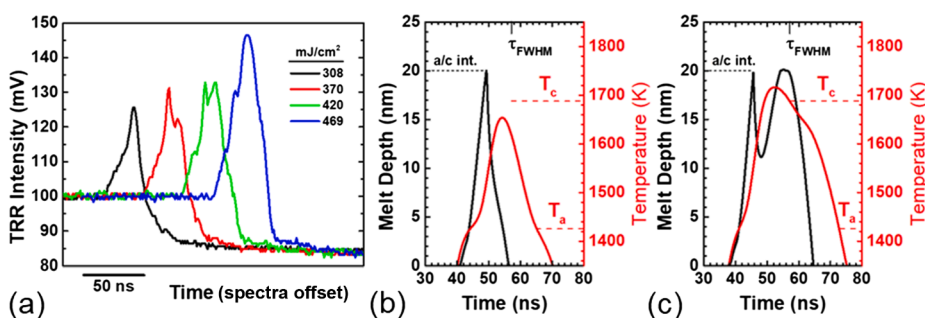

Fig. 5. TRR spectra of laser irradiated a-$Si_{0.7}Ge_{0.3}$ for increasing energy densities progressing from amorphous melting to crystalline melting, (a). Simulation of the time dependent melt depth and temperature profile of a 20 nm a-Si layer where temperatures induced by a single pulse approaches the c-Si melting temperature, (b), and where temperatures surpass the c-Si melting temperature and the melt depth would reach the EOR crystalline region for implanted Si, (c). The process regime of (b) produces the TRR trace observed for the 370 mJ/cm^2 pulse in a-$Si_{0.7}Ge_{0.3}$. and the regime of (c) produces the TRR trace for the 469 mJ/cm^2 pulse.
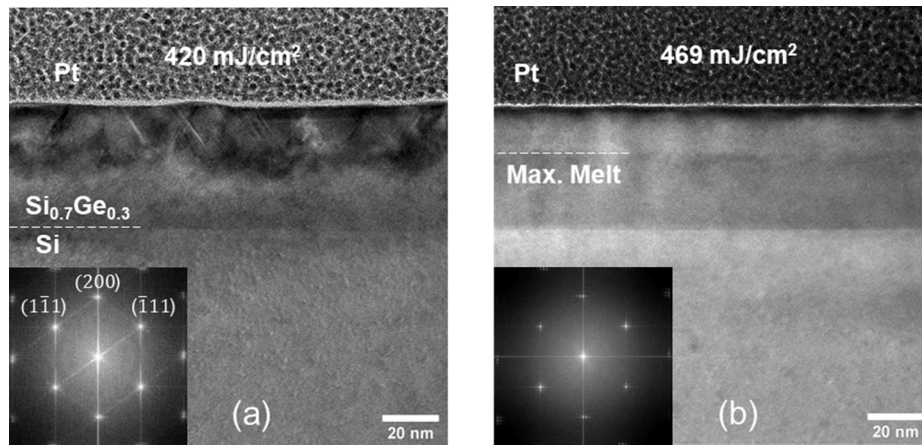
Fig. 6. Cross-sectional TEM image of the amorphized $Si_{0.7}Ge_{0.3}$ film irradiated with a single 420 mJ/cm^2 pulse producing temperatures at the threshold of crystalline melting, (a), and the 469 mJ/cm^2 pulse where the melt propagated through the entire a/c interface, (b).
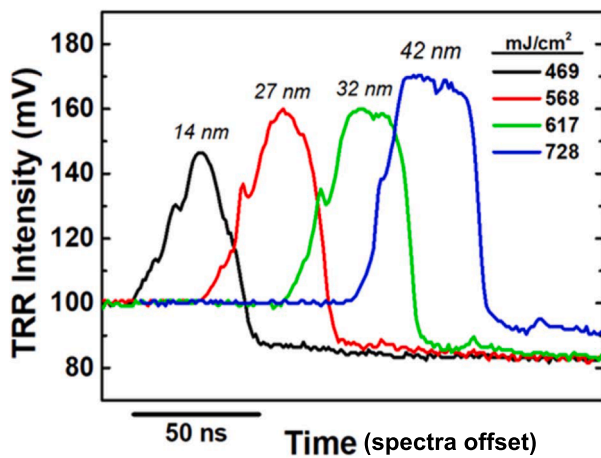

Fig. 7. TRR spectra (offset on the time scale) of amorphized $Si_{0.7}Ge_{0.3}$ laser irradiated with increasing energy densities progressing from EOR defect-free liquid phase epitaxy to full melting of the $Si_{0.7}Ge_{0.3}$ layer.

regions of the image correspond to elements of higher atomic number. The atomic resolution HAADF-STEM image of the 617 mJ/cm^2 pulse in Fig. 9a shows that the clusters are in fact Ge rich. Two EDS scans, shown in Fig. 9b, taken through the middle and outside of a cluster quantitatively shows a significant degree of lateral germanium segregation

occurred during solidification, resulting in a 9% difference in Ge concentration at the surface. A closer inspection of the lateral differences in microstructure near the surface is featured in the HR-TEM image of Fig. 10, where Fourier-filtered images using the primary reflections {200}, {220}, and {111} were used to view regions 1 and 2. Region 1 corresponding to the Ge-poor lattice shows a defect-free matrix with clearly resolved atomic columns, and region 2 shows the disordered Ge-rich lattice. Because of the mixed nature of the sources of contrast among strain, defects, and Z-contrast, interpretation of the HR-TEM image in region 2 is difficult. However, (022) dark-field imaging under g,3g weak-beam conditions show that the defects at the surface are composed of either dislocation half-loops (DHL) or localized dislocation loop (DL) clusters. The formation of the DHLs and DL clusters are most likely strain-relieving in nature as a response to the lateral Ge segregation creating regions with higher lattice mismatch.

The influence of alloy solidification on the l/s interface roughness is made clear by the case of melting to the Si substrate, Fig. 8b., where solidification begins with a perfectly planar l/s interface and microstructural variations are negated due to the homogenized liquid layer seeding from a high purity single component substrate. Molecular dynamics (MD) simulations of the explosive crystallization phenomenon in a-SiGe showed that l/s interface roughness develops in samples with Ge concentrations less than 20% [37]. Coupled with experimental evidence showing that l/s interface velocity decreases with increasing Ge concentration, the MD simulations showed that l/s interface roughening develops due to localized slowing of the l/s interface from the larger Ge atoms being incorporating into the lattice. Furthermore, it was found that the l/s interface planarity was recovered in samples with Ge
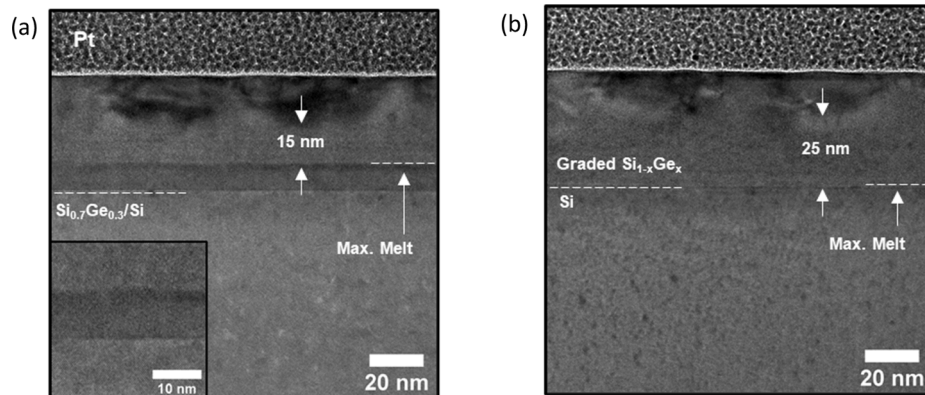

Fig. 8. Cross sectional TEM images of the partially melted $Si_{0.7}Ge_{0.3}$ layer produced with a 617 mJ/cm^2 pulse, (a), and full melting of the layer with a 728 mJ/cm^2 pulse, (b).

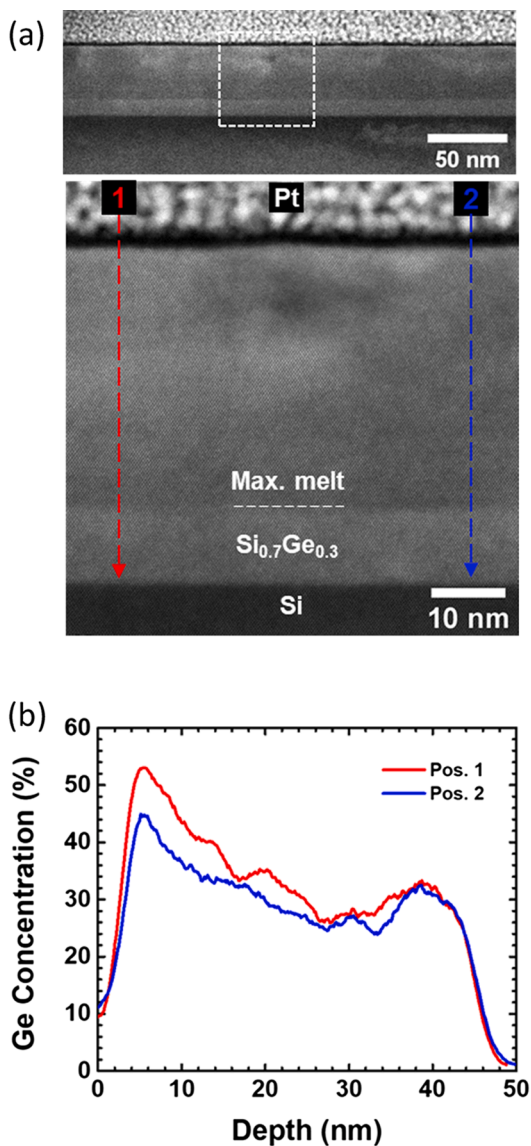**Fig. 9.** HAADF-STEM image of the partially melted $Si_{0.7}Ge_{0.3}$ layer from a single 617 mJ/cm^2 pulse showing the boundary of a Ge rich cluster, (a), and the corresponding EDS line scans inside and outside of the cluster, (b).

concentrations greater than 20–25%. For the samples in this study, the EDS profiles in Fig. 9 shows that lateral deviation in Ge concentration begins at ∼ 25%. This contrast with the MD studies may arise from the difference between pseudomorphic and polycrystalline solidification, in addition to a-SiGe melting versus c-SiGe melting, implying that l/s interface stability may be dependent on the degree of undercooling in the melt in addition to Ge concentration. Strain-relieving defect formation is well studied in SiGe alloys; however, the lateral Ge segregation phenomenon during pulsed laser melt induced epitaxy has yet to be reported in literature. Luong et al in a study of LTP Arsenic-implanted $Si_{0.64}Ge_{0.36}$ using a 248 nm excimer laser with a 20 ns pulse reported similar clustering as this study; however, it was attributed to As clustering based only on HR-TEM observation [27]. A series of microstructural studies by Dagault et al explored LTP of undoped $Si_{0.8}Ge_{0.2}$ layers without amorphizing implants and did not find clustering in the partial to full melting regimes despite reporting significant areas of l/s interface roughness at the maximum melt depth. EDS and SIMS profiles showed that Ge concentrations of ∼ 25% were not reached until a few nm from the surface [38–40]. These findings along with this study seem to suggest that for pseudomorphic liquid phase epitaxy, the onset of l/s
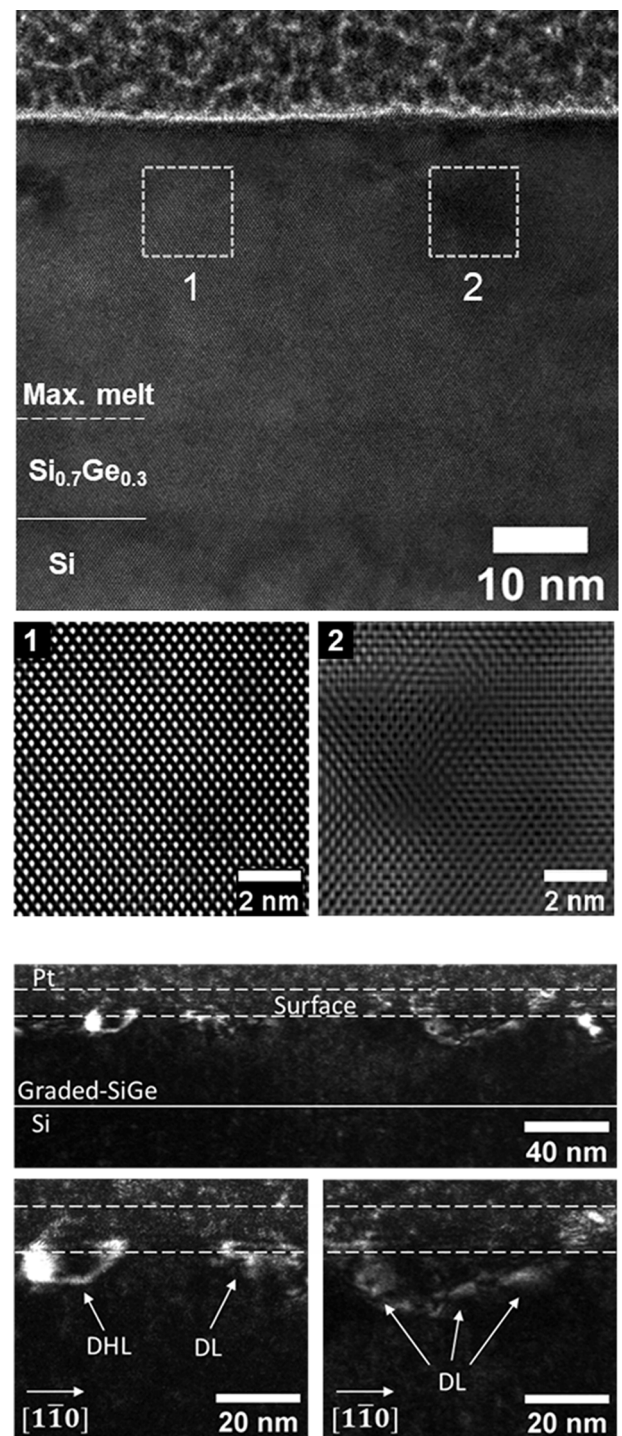

Fig. 10. HR-TEM image of the 617 mJ/cm^2 sample with Fourier-filtered images of the parent matrix in region 1 and the Ge-rich disordered lattice in region 2. (022) Weak-beam dark-field imaging shows the source of lattice disorder is from dislocation half-loops and dislocation loop clusters.

interface instability begins at ∼ 25% Ge. The results of this study can be summarized by Fig. 11 showing the defect evolution for $Si_{0.7}Ge_{0.3}$ as a function of melt depth. Further in-depth studies are needed to understand the evolution of l/s interface roughness during pulsed laser melting of pseudomorphic SiGe layers and elucidate the dependence on Ge concentration, particularly how it leads to the unique coupling of defect clusters with lateral germanium segregation.
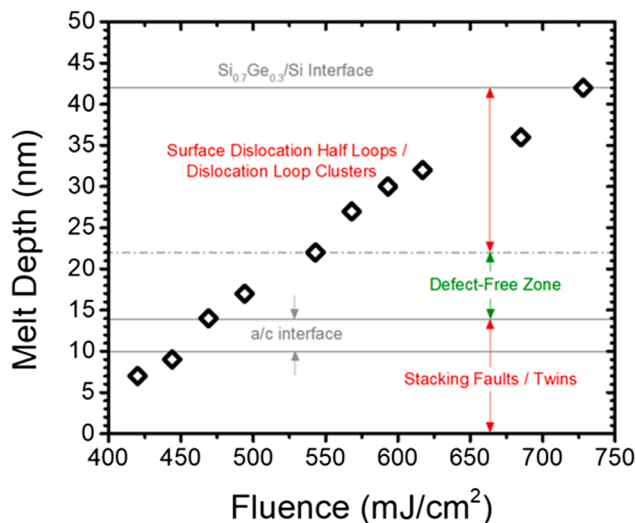
Fig. 11. Plot of melt depth as a function of fluence for implant amorphized $Si_{0.7}Ge_{0.3}$ highlighting the quality of the liquid phase epitaxy.

4. Conclusions

This has been a systematic study of the in situ TRR response and localized microstructural evolution for the pulse laser melting of implant amorphized $Si_{1-x}Ge_x/Si$ thin films. By taking advantage of the variations in reflectance ($\lambda = 658$ nm) between the amorphous, polycrystalline, and single crystal phases of $Si_{1-x}Ge_x$ for Ge concentrations $\leq 50\%$, the solidification regimes between solid phase and liquid phase epitaxy can be resolved as a function of energy density. Moreover, the TRR technique has strong depth resolution in thin (25 nm) liquid SiGe layers. This allowed for monitoring of the l/s interface position through the transition from amorphous melting and solidification, to crystalline melting that occurs in a single pulse at energy densities high enough to reach the crystalline SiGe melting temperature. Time dependent molten depth and temperature profiles of a-Si layers (20 nm) obtained by simulation help explain the TRR results.

End-of-Range defect free liquid phase epitaxy was achieved when the melt front propagated past the damaged crystalline region at the a/c interface without forming any extended defects in the SiGe layer or underlying Si substrate. The ideal process window for pulsed laser melting of implant amorphized SiGe is between the energy density that produces EOR defect-free liquid phase epitaxy and melting to the $Si_{1-x}Ge_x/Si$ interface. Progressive l/s interface roughening during solidification leads to significant lateral germanium segregation coupled with dislocation half-loop and dislocation loop cluster formation in the Ge-rich regions after $\sim$ 22 nm of liquid phase epitaxy in the $Si_{0.7}Ge_{0.3}$ thin films. If solidification is limited to less than this distance, then defect free epitaxy is observed to occur.

CRediT authorship contribution statement

Jesse A. Johnson II: Writing - original draft, Methodology, Data curation, Investigation. **David Brown:** Writing - review & editing, Investigation. **Emily Turner:** Data curation. **Chris Hatem:** Funding acquisition, Investigation. **Bruce Adams:** Investigation, Methodology. **Xuebin Li:** Investigation. **Kevin S. Jones:** Writing - review & editing, Methodology, Funding acquisition.

Declaration of Competing Interest

The authors declare that they have no known competing financial interests or personal relationships that could have appeared to influence the work reported in this paper.

Appendix A. Supplementary material

Supplementary data to this article can be found online at https://doi.org/10.1016/j.apsusc.2021.150408.

References

[1] S.E. Thompson, M. Armstrong, C. Auth, M. Alavi, M. Buehler, R. Chau, S. Cea, T. Ghani, G. Glass, T. Hoffman, C.H. Jan, C. Kenyon, J. Klaus, K. Kuhn, Z. Ma, B. Mcintyre, K. Mistry, A. Murthy, B. Obradovic, R. Nagisetty, P. Nguyen, S. Sivakumar, R. Shaheed, L. Shifren, B. Tufts, S. Tyagi, M. Bohr, Y. El-Mansy, A 90-nm logic technology featuring strained-silicon, IEEE Trans. Electron Devices. 51 (2004) 1790–1797, https://doi.org/10.1109/TED.2004.836648.

[2] K.W. Ang, K. Majumdar, K. Matthews, C.D. Young, C. Kenney, C. Hobbs, P.D. Kirsch, R. Jammy, R.D. Clark, S. Consiglio, K. Tapily, Y. Trickett, G. Nakamura, C.S. Wajda, G.J. Leusink, M. Rodgers, S.C. Gausepohl, Effective Schottky Barrier Height modulation using dielectric dipoles for source/drain specific contact resistivity improvement, Tech. Dig. - Int. Electron Devices Meet. IEDM. (2012) 18.6.1–18.6.4, https://doi.org/10.1109/IEDM.2012.6479068.

[3] P. Raghavan, M.G. Bardon, D. Jang, P. Schuddinck, D. Yakimets, J. Ryckaert, A. Mercha, N. Horiguchi, N. Collaert, A. Mocuta, D. Mocuta, Z. Tokei, D. Verkest, A. Thean, A. Steegen, Holisitic device exploration for 7nm node, Proc. Cust. Integr, Circuits Conf. 2015-Novem (2015) 2–6, https://doi.org/10.1109/CICC.2015.7338377.

[4] R. Hung, F.A. Khaja, K.E. Hollar, K.V. Rao, S. Munnangi, Y. Chen, M. Okazaki, Y.C. Huang, X. Li, H. Chung, O. Chan, C. Lazik, M. Jin, H. Zhou, A. Mayur, N. Kim, E. Yieh, Novel solutions to enable contact resistivity <1E-9 Ω-cm2for 5nm node and beyond, 2018 Int, Symp. VLSI Technol. Syst. Appl. VLSI-TSA 2018 (2018) 1–2, https://doi.org/10.1109/VLSI-TSA.2018.8403817.

[5] O. Gluschenkov, H. Jagannathan, (Invited) Laser Annealing in CMOS Manufacturing, ECS Trans. 85 (2018) 11–23, https://doi.org/10.1149/08506.0011ecst.

[6] K. Itoh, Y. Sasaki, T. Mitsuishi, M. Miyao, M. Tamura, Thermal behavior of b, p and as atoms in supersaturated si produced by ion implantation and pulsed-laser annealing, Jpn. J. Appl. Phys. 21 (1982) L245–L247, https://doi.org/10.1143/JJAP.21.L245.

[7] S. Talwar, Junction scaling using lasers for thermal annealing (2003) 83–86.

[8] A. Shima, Laser annealing technology and device integration challenges, ICSICT-20068th Int, Conf. Solid-State Integr. Circuit Technol. Proc. 2006 (2006) 454–457, https://doi.org/10.1109/ICSICT.2006.306299.

[9] J.L. Everaert, M. Schaekers, H. Yu, L.L. Wang, A. Hikavyy, L. Date, J. Del Agua Borniquel, K. Hollar, F.A. Khaja, W. Aderhold, A.J. Mayur, J.Y. Lee, H. Van Meer, Y.L. Jiang, K. De Meyer, D. Mocuta, N. Horiguchi, Sub-10-9Ω·cm2contact resistivity on p-SiGe achieved by Ga doping and nanosecond laser activation, Dig. Tech. Pap. - Symp. VLSI Technol. 36 (2017) T214–T215, https://doi.org/10.23919/VLSIT.2017.7998176.

[10] M.Y. Tsai, B.G. Streetman, Recrystallization of implanted amorphous silicon layers. I. Electrical properties of silicon implanted with BF+2 or Si ++B+, J. Appl. Phys. 50 (1979) 183–187, https://doi.org/10.1063/1.325688.

[11] P. Baeri, S.U. Campisano, G. Foti, E. Rimini, A melting model for pulsing-laser annealing of implanted semiconductors, J. Appl. Phys. 50 (1979) 788–797, https://doi.org/10.1063/1.326046.

[12] Y. Takamura, P.B. Griffin, J.D. Plummer, Y. Takamura, P.B. Griffin, J.D. Plummer, Physical processes associated with the deactivation of dopants in laser annealed silicon Physical processes associated with the deactivation of dopants in laser annealed silicon, J. Appl. Phys. 235 (2002), https://doi.org/10.1063/1.1481974.

[13] R. Murto, K. Jones, M. Rendon, S. Talwa, Activation and deactivation studies of laser thermal annealed boron, arsenic, phosphorus, and antimony ultra-shallow abrupt junctions, Proc. Int. Conf. Ion Implant. Technol. (2000) 155–158, https://doi.org/10.1109/.2000.924113.

[14] A. Matsuno, K. Shibahara, Effect of pulse duration on formation of ultrashallow junction by excimer laser annealing, Japanese J. Appl. Physics, Part 1 Regul. Pap. Short Notes Rev. Pap. 45 (2006) 8537–8541, https://doi.org/10.1143/JJAP.45.8537.

[15] M.O. Thompson, G.J. Galvin, J.W. Mayer, P.S. Peercy, J.M. Poate, D.C. Jacobson, A.G. Cullis, N.G. Chew, Melting temperature and explosive crystallization of amorphous silicon during pulsed laser irradiation, Phys. Rev. Lett. 52 (1984) 2360–2363, https://doi.org/10.1103/PhysRevLett.52.2360.

[16] A. Shima, H. Ashihara, T. Mine, Y. Goto, M. Horiuchi, Y. Wang, S. Talwar, A. Hiraiwa, Self-limiting laser thermal process for ultra-shallow junction formation

of 50-nm gate CMOS, IEEE Int. Electron Devices Meet. (2003) 20.4.1--20.4.4, https://doi.org/10.1109/IEDM.2003.1269329.

[17] M. Berti, G. Mazzi, L. Calcagnile, A.V. Drigo, P.G. Merli, A. Migliori, Composition and structure of Si-Ge layers produced by ion implantation and laser melting, J. Mater. Res. 6 (1991) 2120–2126, https://doi.org/10.1557/JMR.1991.2120.

[18] J.M.C. Stork, G.L. Patton, E.F. Crabbe, D.L. Harame, B.S. Meyerson, S.S. Iyer, E. Ganin, Design Issues for SiGe Heterojunction Bipolar Transistors, Proc. Bipolar Circuits Technol. Meet. (1989) 57–64, https://doi.org/10.1109/BIPOL.1989.69460.

[19] S. Lombardo, K. Kramer, M.O. Thompson, D.R. Smith, Pulsed laser assisted epitaxy of GexSi1-x alloys on Si (100), Appl. Phys. Lett. 59 (1991) 3455–3457, https://doi.org/10.1063/1.105676.

[20] M. Berti, G. Mazzi, A.V. Drigo, A. Migliori, E. Jannitti, S. Nicoletti, Laser Induced Epitaxial Regrowth of Si1-xG ex / S i Layers Produced By Ge Ion Implantation, Appl. Surf. Sci. 43 (1989) 158–164.

[21] D.P. Brunco, M.O. Thompson, D.E. Hoglund, M.J. Aziz, H.J. Gossmann, Germanium partitioning in silicon during rapid solidification, J. Appl. Phys. 78 (1995) 1575–1582, https://doi.org/10.1063/1.360251.

[22] C.Y. Ong, K.L. Pey, X. Li, X.C. Wang, C.M. Ng, L. Chan, Laser annealing induced high Ge concentration epitaxial SiGe layer in Si1-x Gex virtual substrate, Appl. Phys. Lett. 93 (2008) 2006–2009, https://doi.org/10.1063/1.2962991.

[23] O. Gluschenkov, H. Wu, K. Brew, C. Niu, L. Yu, Y. Sulehria, S. Choi, C. Durfee, J. Demarest, A. Carr, S. Chen, J. Willis, T. Thanigaivelan, F.L. Lie, W. Kleemeier, D. Guo, External Resistance Reduction by Nanosecond Laser Anneal in Si/SiGe CMOS Technology, Tech. Dig. - Int. Electron Devices Meet. IEDM. (2018-Decem (2019)) 35.3.1--35.3.4, https://doi.org/10.1109/IEDM.2018.8614628.

[24] C.Y. Chang, F.A. Khaja, K.E. Hollar, K. V. Rao, C. Lazik, M. Jin, H. Zhou, R. Hung, Y.C. Huang, H. Chung, A. Mayur, N. Kim, Ultra-low (1.2×10-9Ωcm2) p-Si0.55Ge0.45contact resistivity (ρc) using nanosecond laser anneal for 7nm nodes and beyond, 17th Int. Work. Junction Technol. IWJT 2017. 2 (2017) 23–26. https://doi.org/10.23919/IWJT.2017.7966504.

[25] T. Tabata, J. Aubin, K. Huet, F. Mazzamuto, Segregation and activation of Ga in high Ge content SiGe by UV melt laser anneal, J. Appl. Phys. 125 (2019), https://doi.org/10.1063/1.5096889.

[26] T. Tabata, J. Aubin, K. Huet, F. Mazzamuto, Y. Mori, A. La Magna, L.M. Rubin, P. Kopalidis, H.C. Tsai, D. Roh, R. Reece, Super Activation of Highly Surface Segregated Dopants in High Ge Content SiGe Obtained by Melt UV Laser Annealing, Proc. Int. Conf. Ion Implant. Technol. (2018-Septe (2018)) 353–356, https://doi.org/10.1109/IIT.2018.8807912.

[27] G.V. Luong, S. Wirths, S. Stefanov, B. Holländer, J. Schubert, J.C. Conde, T. Stoica, U. Breuer, S. Chiussi, M. Goryll, D. Buca, S. Mantl, Study of dopant activation in biaxially compressively strained SiGe layers using excimer laser annealing, J. Appl. Phys. 113 (2013), https://doi.org/10.1063/1.4807001.

[28] D.H. Lowndes, S.J. Pennycook, G.E. Jellison, S.P. Withrow, D.N. Mashburn, Solidification of highly undercooled liquid silicon produced by pulsed laser melting of ion-implanted amorphous silicon: Time-resolved and microstructural studies, J. Mater. Res. 2 (1987) 648–680, https://doi.org/10.1557/JMR.1987.0648.

[29] T.M. Donovan, E.J. Ashley, H.E. Bennett, Effect of Surface Damage on the Reflectance of Germanium in the 2650–10 000-Å Region, J. Opt. Soc. Am. 53 (1963) 1403, https://doi.org/10.1364/josa.53.001403.

[30] M.O. Thompson, Liquid-Solid Interface Dynamics During Pulsed Laser Melting of Silicon-On-Sapphire, Cornell University, 1984.

[31] H.C. Webber, A.G. Cullis, N.G. Chew, Computer simulation of high speed melting of amorphous silicon, Appl. Phys. Lett. 43 (1983) 669–671, https://doi.org/10.1063/1.94440.

[32] M.J. Aziz, C.W. White, J. Narayan, B. Stritzker, Melting of Crystalline and Amorphous Silicon by Ruby, XeCl, and KrF Laser Irradiation, Ed. La Phys IV (1985) 231–236.

[33] C. Cayron, M. Den Hertog, L. Latu-Romain, C. Mouchet, C. Secouard, J.L. Rouviere, E. Rouviere, J.P. Simonato, Odd electron diffraction patterns in silicon nanowires and silicon thin films explained by microtwins and nanotwins, J. Appl. Crystallogr. 42 (2009) 242–252, https://doi.org/10.1107/S0021889808042131.

[34] J.P. Dismukes, L. Ekstrom, Homogeneous solidification of Ge-Si alloys, Trans. Metall. Soc. AIME. 233 (1965) 672–680.

[35] Y.F. Chong, K.L. Pey, A.T.S. Wee, T. Osipowicz, A. See, L. Chan, Control of transient enhanced diffusion of boron after laser thermal processing of preamorphized silicon, J. Appl. Phys. 92 (2002) 1344–1350, https://doi.org/10.1063/1.1491278.

[36] G.E. Jellison Jr., D.H. Lowndes, R.F. Wood, Fundamental Aspects Of Pulsed-Laser Irradiation Of Semiconductors, Excimer Lasers Opt. 0710 (1987) 24, https://doi.org/10.1117/12.937293.

[37] E.J. Albenze, M.O. Thompson, P. Clancy, Molecular dynamics study of explosive crystallization of SiGe and boron-doped SiGe alloys, Ind. Eng. Chem. Res. 45 (2006) 5628–5639, https://doi.org/10.1021/ie051361w.

[38] L. Dagault, P. Acosta-Alba, S. Kerdilès, J.-P. Barnes, J.-M. Hartmann, P. Gergaud, T. T. Nguyen, A. Grenier, J. Aubin, F. Cristiano, Composition and Strain Evolution of Undoped Si 0.8 Ge 0.2 Layers Submitted to UV-Nanosecond Laser Annealing, ECS Trans. 86 (2018) 29–39, https://doi.org/10.1149/08607.0029ecst.

[39] L. Dagault, P. Acosta-Alba, S. Kerdilès, J.P. Barnes, J.M. Hartmann, P. Gergaud, T. T. Nguyen, A. Grenier, A.M. Papon, N. Bernier, V. Delaye, J. Aubin, F. Cristiano, Impact of UV Nanosecond Laser Annealing on Composition and Strain of Undoped Si 0.8 Ge 0.2 Epitaxial Layers, ECS J. Solid State, Sci. Technol. 8 (2019) P202–P208, https://doi.org/10.1149/2.0191903jss.

[40] L. Dagault, S. Kerdilès, P. Acosta Alba, J.M. Hartmann, J.P. Barnes, P. Gergaud, E. Scheid, F. Cristiano, Investigation of recrystallization and stress relaxation in nanosecond laser annealed Si1−xGex/Si epilayers, Appl. Surf. Sci. 527 (2020), 146752, https://doi.org/10.1016/j.apsusc.2020.146752.